

RESEARCH ARTICLE

NANOFUIDICS

Neuromorphic functions with a polyelectrolyte-confined fluidic memristor

Tianyi Xiong^{1,2}, Changwei Li^{1,3}, Xiulan He¹, Boyang Xie^{1,2}, Jianwei Zong^{1,2}, Yanan Jiang⁴, Wenjie Ma¹, Fei Wu¹, Junjie Fei³, Ping Yu^{1,2*}, Lanqun Mao^{1,4*}

Reproducing ion channel-based neural functions with artificial fluidic systems has long been an aspirational goal for both neuromorphic computing and biomedical applications. In this study, neuromorphic functions were successfully accomplished with a polyelectrolyte-confined fluidic memristor (PFM), in which confined polyelectrolyte-ion interactions contributed to hysteretic ion transport, resulting in ion memory effects. Various electric pulse patterns were emulated by PFM with ultralow energy consumption. The fluidic property of PFM enabled the mimicking of chemical-regulated electric pulses. More importantly, chemical-electric signal transduction was implemented with a single PFM. With its structural similarity to ion channels, PFM is versatile and easily interfaces with biological systems, paving a way to building neuromorphic devices with advanced functions by introducing rich chemical designs.

The development of artificial systems with brainlike functions (i.e., neuromorphic devices) is rapidly expanding because of their promising applications in neuromorphic computing (1, 2), bioinspired sensorimotor implementation (3, 4), brain-machine interfaces (5, 6), and neuroprosthetics (7, 8). So far, neuromorphic functions with diverse patterns have been achieved and incorporated into applications in various ways, mainly with history-dependent solid-state resistance-switchable devices, including two-terminal memristors (9–11) and three-terminal transistors (12, 13). However, most of the neuromorphic functions achieved thus far are based on the emulation of the electric pulse pattern using solid-state devices. An analog to the biological synapse—especially the emulation of a chemical synapse in a solution-based context—remains very challenging with these solid-state devices. In this regard, a fluidic-based memristor is highly desirable to achieve neuromorphic functions in an aqueous environment, because of its superior compatibility with biological systems and the larger number of functions endowed to the neuromorphic devices by introducing diverse chemistries (14).

Previous attempts have revealed that ion-based micro- or nanofluidic devices with

advanced functionalities [e.g., the ion diode (15), ion transistor (16), or ion switch (17)] are achievable by confining an electrolyte into micro- or nanochannels. Several studies reported that these confined systems feature memresistance and memcapacitance (18–20). Moreover, long-term plasticity was obtained with nanochannels by introducing an ionic liquid-electrolyte interface (21). Despite these efforts, realizing neuromorphic functions in aqueous media is still a long-standing challenge, mainly because the strong shielding effect in an aqueous environment greatly hinders interionic interactions, thereby limiting the formation of memory in fluidic-based systems. In 2021, a milestone theoretical model predicted that ion memory functions could be accomplished with two-dimensional extremely confined channels (22), which has been experimentally realized by the same group (23).

Here, we report a polyelectrolyte-confined fluidic memristor (PFM) that can successfully accomplish various neuromorphic functions for mimicking not only electric pulse patterns but also chemical-electric signal transduction. Inspired by biological ion channels that function as natural memristors by controlling ion flux with spatial confinement and molecular recognition (24) (Fig. 1A), we designed and fabricated a polyimidazolium brush (PimB)-confined fluidic channel (Fig. 1B). We selected polyimidazolium because of its high charge density, rich chemistry, and versatile ability to recognize different anions (25). Typically, PimBs were grown onto the inner wall of the glass micro- or nanopipette by surface-initiated atomic transfer radical polymerization (26) (fig. S1, A and B). In this way, the fluid was confined by PimBs, in which the

establishment of anion concentration equilibrium and charge balance between the inside and outside of PimBs under the stimulation of electric fields or chemicals would be hysteretic, resulting in history-dependent ion memory.

Polyelectrolyte-confined fluidic memristor

The device was constructed by a PimB-confined conically fluidic channel, an electrolyte, and, to complete the electric connection, two Ag/AgCl electrodes (fig. S1C). A triangle wave voltage was applied to the device to investigate the current-voltage (*I*-*V*) relationship. The rectified *I*-*V* curve was recorded with a modified micropipette (Fig. 1C, red) because of the geometric asymmetry of the conical channel and the anion selectivity of the positively charged PimB (26). Meanwhile, the pinched *I*-*V* curve collected under this periodic voltage with a nonzero cross-point voltage (V_{cp}) satisfied the history-dependent memristor nature according to Chua's theory (27). This offset (V_{cp}) originates from the influence of surface charge in this asymmetric channel (28), which is usually observed for biological memristors, such as the K⁺ ion channel (29). In contrast, the bare micropipette only yields the linear ohmic *I*-*V* curve (Fig. 1C, blue), demonstrating the essential role of PimB in this pinched hysteretic loop.

We further investigated the dependence of current on voltage scanning frequency (i.e., scan rates, v). The *I*-*V* curve experiences a transition from the hysteretic and rectified form at lower scan rates to the linear-like form at higher scan rates (Fig. 1D and fig. S2). The area (S) inside the hysteresis loop shrinks as the scan rate increases and degenerates to zero at infinite scan rate, as suggested by the fitting of the S - v relationship (Fig. 1E and supplementary text). The pinched hysteresis loop, reduced loop area with increasing frequency, and the linear *I*-*V* relationship under infinite frequency satisfy three fingerprints of a memristor (29).

To explore the origin of memristive behavior of the PFM, we conducted dynamic monitoring of ion conductivity under different constant bias voltages (Fig. 1F). At a voltage equal to V_{cp} (53 mV), PFM maintains a static ion conductivity over time (Fig. 1F, yellow). At a voltage higher than V_{cp} (200 mV), the conductivity gradually increases to reach a plateau in ~2 s (Fig. 1F, red), whereas it decreases to leveling in 1 s at a voltage lower than V_{cp} (~200 mV) (Fig. 1F, blue). These results confirm that the ion conductivity change of PFM is a time-dependent process.

The conductivity change is closely associated with ion dynamic distribution inside the channel. We carried out finite element modeling (FEM) to describe the changes of ion distribution over time under different bias voltages (supplementary text and fig. S3A).

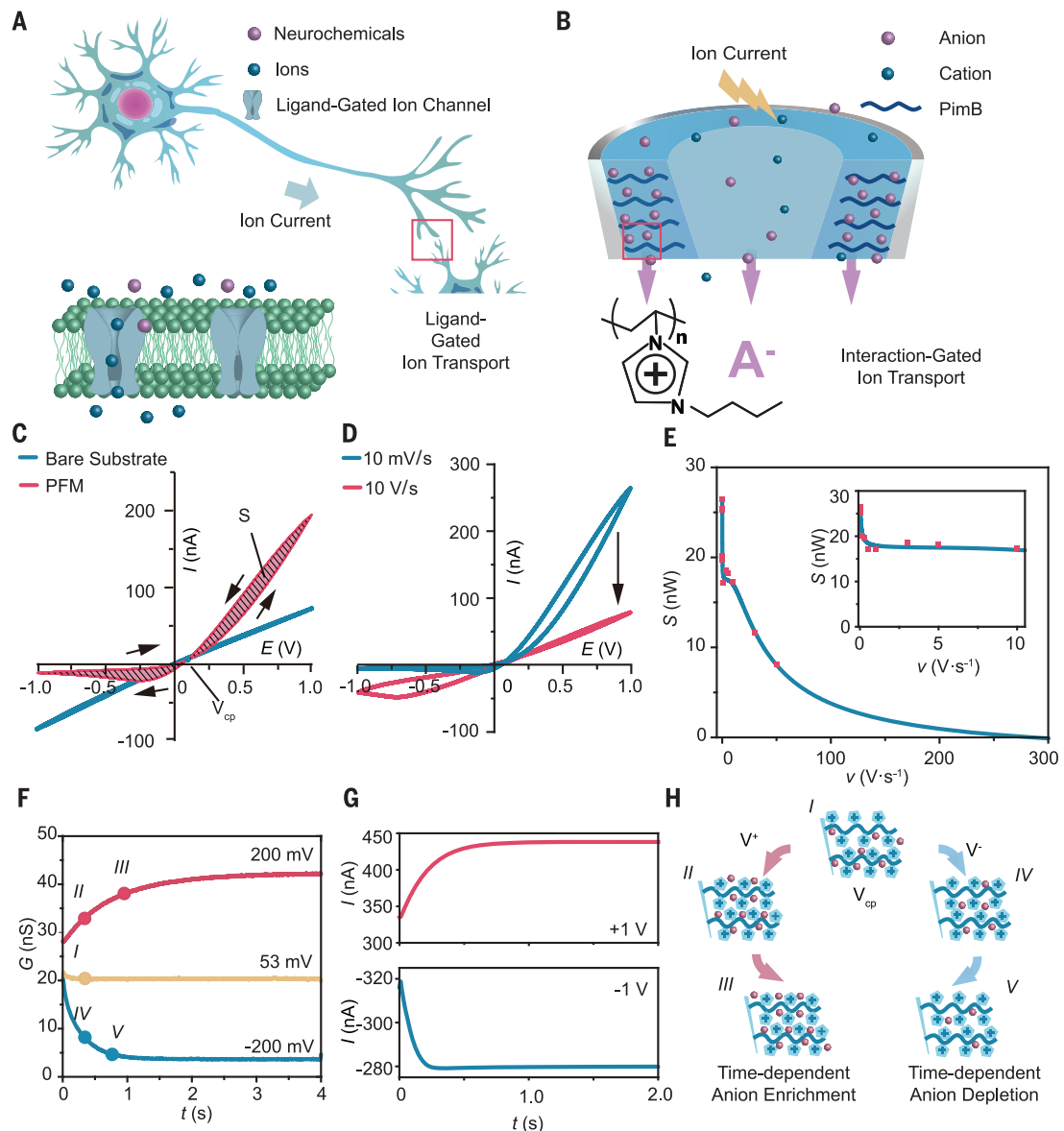
¹Beijing National Laboratory for Molecular Sciences, Key Laboratory of Analytical Chemistry for Living Biosystems, Institute of Chemistry, Chinese Academy of Sciences (CAS), Beijing 100190, China. ²School of Chemical Sciences, University of Chinese Academy of Sciences, Beijing 100049, China.

³Key Laboratory of Environmentally Friendly Chemistry and Applications of Ministry of Education, College of Chemistry, Xiangtan University, Xiangtan 411105, China. ⁴College of Chemistry, Beijing Normal University, Beijing 100875, China.

*Corresponding author. Email: yuping@iccas.ac.cn (P.Y.); lqmao@bnu.edu.cn (L.M.)

Fig. 1. Conductivity changes of PFM. (A and B) Schematic illustration of the neural functions realized by interaction-gated ion current in biological neurons (A) and a PimB-confined fluidic system (B). (C) $I-V$ curves of PFM (red) and a bare micropipette (blue) in 10 mM KCl aqueous solution under a triangle wave with a scan rate of 50 mV/s. The hysteresis loop area is shaded in purple. The arrows show the scan direction. (D) $I-V$ curves of PFM in 10 mM KCl under triangle waves with a fast (10 V/s, red) and a slow (10 mV/s, blue) scan rate. (E) Plot of the hysteresis loop area (S) with scan rate (v). (Inset) Zoom-in of the plot at low-scan rate. (F) Time-dependent conductivity changes of PFM in 10 mM KCl under a constant bias voltage equal to V_{cp} (53 mV, yellow), higher than V_{cp} (+200 mV, red), and lower than V_{cp} (-200 mV, blue).

(G) Simulated $I-t$ curves of PFM in 10 mM KCl under +1 V (top) and -1 V (bottom) bias voltages. (H) Schematic illustration of time-dependent ion redistribution processes in PFM at potentials higher than V_{cp} (from I to III) and lower than V_{cp} (from I to V).



Without a bias voltage, cation (K^+) and anion (Cl^-) concentrations in the bulk layer are balanced to maintain charge neutrality, which are equal to the bulk electrolyte concentration (fig. S3B). While in the positively charged PimB layer, Cl^- ions overwhelm K^+ ions with a high concentration (~104.5 mM) owing to the strong electrostatic attraction between anions and the imidazolium moieties (fig. S3B). This high surface charge density of the PimB confers large anion storage, and the anions in PimB have relatively slow diffusion dynamics, necessitating prolonged enrichment of Cl^- in the PimB layer from the rest state to reach steady ion distribution at +1 V (Fig. 1H and fig. S3C). Therefore, the ion current undergoes a gradual increase to its steady state (Fig. 1G, red). Similarly, the slowed depletion of Cl^- in the PimB layer at -1 V (Fig. 1H and fig. S3D)

results in the gradual decrease of ion current (Fig. 1G, blue). These simulated consequences match well the temporal profiles of ion conductivity at constant bias potentials (Fig. 1F), suggesting that the relatively slow diffusion dynamics of anions into and out of the PimBs leads to time-dependent ion memory and, consequently, the memristive behavior of the device.

Mimicking short-term plasticity patterns with PFM

To mimic short-term plasticity (STP) electric pulse patterns, we applied paired voltage pulses to the PFM and recorded current spikes in accordance with pulsed stimulations. As shown, two continuous pulses of +2 or -2 V induce a current increase ($\Delta I = 8.9$ nA), called a paired-pulse facilitation (PPF; Fig. 2A), or a signifi-

cant current decline ($\Delta I = -48.4$ nA), called a paired-pulse depression (PPD; Fig. 2B), validating the capability of PFM in emulating the STP electric pulses. FEM simulation of ion dynamics under the same pulsed voltage waveforms reproduces the similar trends of current change (Fig. 2C), further demonstrating that STP electric pulses originated from time-dependent ion redistribution in PFM. The applied voltage drives the ion concentration polarization in the PimB layer that gives rise to the observed current spike. Upon removal of the external electric field (i.e., at the pulse interval), slow anion diffusion dynamics in the PimB layer would briefly hold the ion concentration polarization state owing to the strong interaction between Pim and anions. Hysteretic ion redistribution during the pulse interval continues to influence the anion enrichment or depletion in

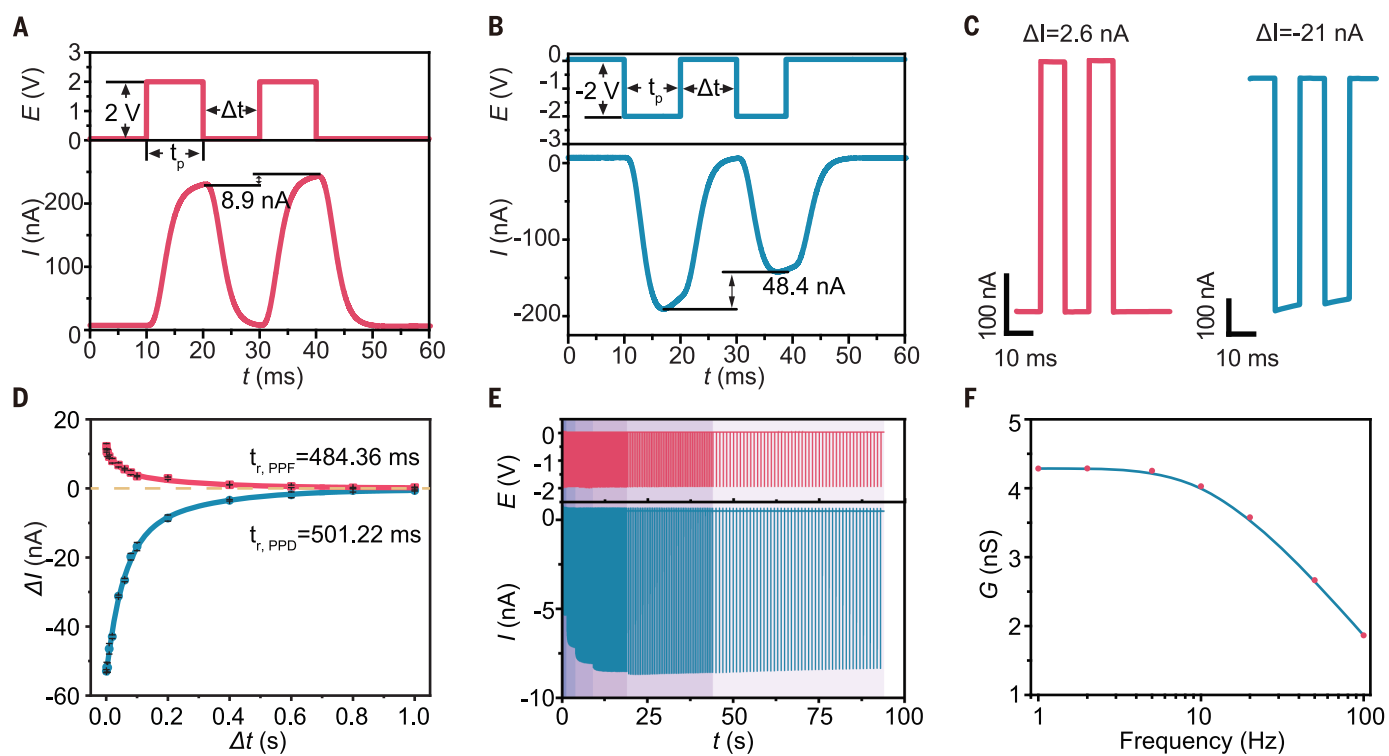


Fig. 2. STP electric pulses of PFM. PPF (A) and PPD (B) of PFM in 10 mM NaCl. The upper plots show voltage pulse waveforms. (C) The simulated I - t responses with FEM under the same voltage waveforms in (A) (red) and (B) (blue). (D) Plots of current changes (ΔI) with the paired pulse intervals (Δt) under positive ($V = +2\text{ V}$, $t_p = 10\text{ ms}$, red) and negative

($V = -2\text{ V}$, $t_p = 10\text{ ms}$, blue) bias voltages. Error bars present standard deviation of three measurements with the same device. (E) Current responses under voltage pulse train ($V = -2\text{ V}$, $t_p = 5\text{ ms}$) with varying frequency from 1 to 100 Hz. (F) Plot of conductivity versus the applied voltage pulse frequency.

the PimB layer when a voltage pulse was applied again, leading to the conductivity (or ion current) level up or down of the next spike, thus enabling the mimicking of STP electric pulses with the PFM. This conductivity change is strongly related to the pulse interval (Δt) following a biexponential relationship

$$\Delta I = A_1 e^{-\left(\frac{\Delta t}{\tau_1}\right)} + A_2 e^{-\left(\frac{\Delta t}{\tau_2}\right)} \quad (1)$$

where τ_1 and τ_2 are two time constants that might be related to the ion redistribution in the bulk and PimB layer, respectively; and A_1 and A_2 are the weights of these two dynamic processes. Shortening of the voltage pulse interval (Δt) leads to increased current change (ΔI), whereas a prolonged voltage pulse interval results in reduced ΔI . This decline dynamics emulates the change of synaptic weight in shaping biological STPs under repeated stimuli of varying frequencies (30). We then calculated the retention time (t_r) of PFM, defined as the pulse interval where ΔI drops to 5% of its maximum ($\Delta I_{\Delta t=t_r} = 5\% \Delta I_{\Delta t=0}$). For a certain voltage pulse stimulation (e.g., $V = \pm 2\text{ V}$, $t_p = 10\text{ ms}$), t_r was calculated to be $\sim 500\text{ ms}$ (Fig. 2D and table S1; $t_r = 484.36\text{ ms}$ for facil-

itation and $t_r = 501.22\text{ ms}$ for depression) in 10 mM NaCl aqueous solution. These values of PFM are comparable to those of STP in biological systems (table S1), where facilitation and depression of the synaptic weight occurs on a 10^2-ms scale (30).

We further validated the ability of the PFM to emulate dynamic filtering functions in sensory neurons. By applying a negative voltage pulse train with the pulse frequency ranging from 1 to 100 Hz ($V = -2\text{ V}$, $t_p = 5\text{ ms}$; Fig. 2E), frequency-dependent conductivity was obtained (Fig. 2F). The minor difference in the frequency of the voltage pulse train (e.g., 19, 20, or 21 Hz) could be differentiated by the conductivity differences with this filtering function (fig. S4). In addition, programming voltage pulses ($V_{\text{set}} = +2\text{ V}$, $V_{\text{reset}} = -0.6\text{ V}$) causes an analog ion conductivity switch among 100 continuous states. The device maintains good performance after 30,000 set-reset tests (fig. S5), demonstrating the endurance of the PFM. Energy consumption (W) of the PFM was calculated on the basis of the integration of I - t responses under single voltage pulses with $W = \int VIdt$, which was closely related to the orifice size of the pipette and the applied voltage (fig. S6, A and B). For a 150-nm-

diameter nanopipette-based device, energy consumption under voltage stimulation of -100 mV ($t_p = \Delta t = 10\text{ ms}$) is 0.66 pJ per spike (fig. S6C), which is close to the biological voltage (-70 mV) and energy consumption (31). In contrast to most of the reported memristors that require high voltages, our PFM can operate at the voltage and energy consumption as low as those biological systems (table S2), demonstrating its potential for application in bio-inspired sensorimotor implementation and neuroprosthetics.

Chemical-regulated STP electric pulses

Neurons work in a complex chemical environment wherein ions and molecules lay the foundations for all neuroactivities. Changes in the chemical environment fundamentally contribute to manifold behaviors of neurons, including synaptic scaling induced by *N*-methyl-D-aspartate (32) and enhanced transmission induced by neurotrophins (33). This chemical modulation effect was emulated with the PFM by tuning the Pim-anion interactions. The I - V curves collected in different electrolyte solution (NaCl, NaBF₄, or NaClO₄) illustrate the dependence of hysteresis loop area (S) on the species of anions (Fig. 3A). We then investigated

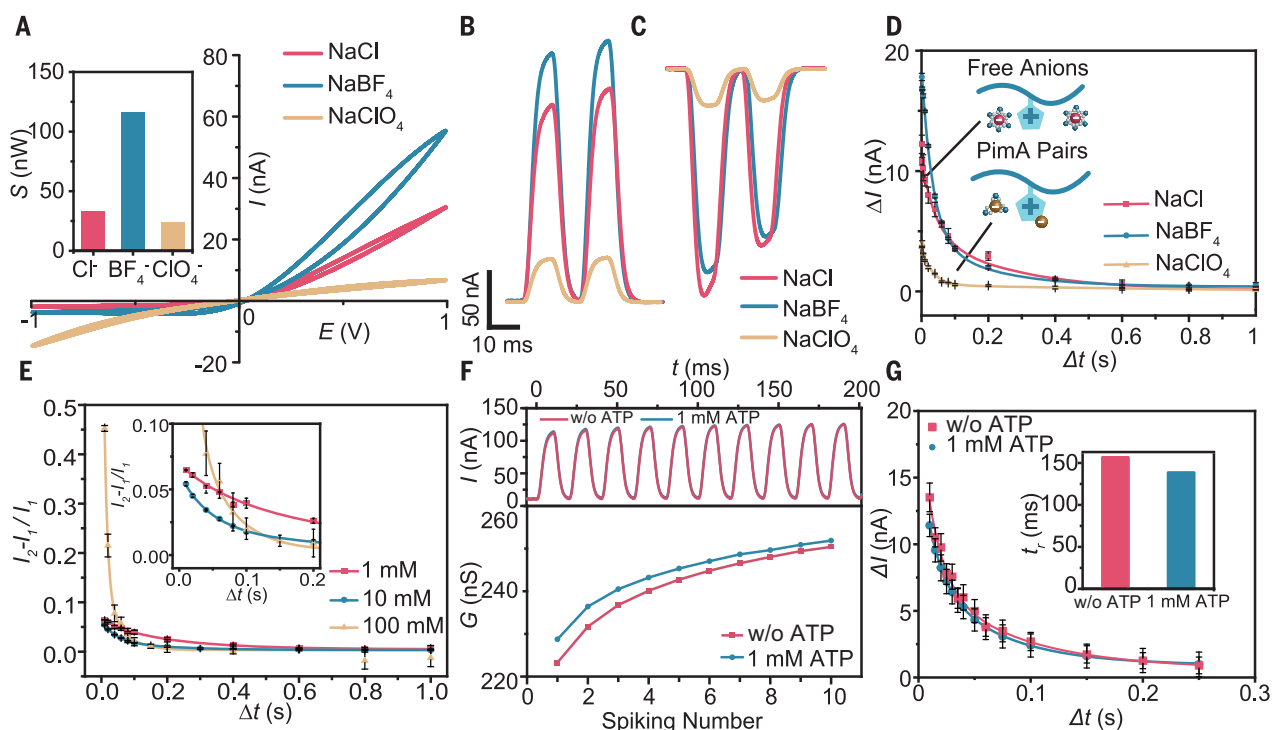


Fig. 3. Chemical-regulated STP electric pulses. (A) I - V curves of PFM in 10 mM NaCl, NaBF₄, or NaClO₄ solution with a scan rate of 50 mV/s. (Inset) The hysteresis loop area (S) from the I - V curves. (B and C) PPF (B) and PPD (C) of PFM in different electrolyte solutions. (D) Plots of current changes with pulse intervals in different electrolyte solution ($V = -2$ V, $t_p = 10$ ms). (Inset) Schematic illustration of free anions and PimA pairs. (E) Plots of normalized current changes with pulse intervals in KCl solutions with different concentrations

($V = -2$ V, $t_p = 10$ ms). (Inset) Zoom-in of the plot at short pulse intervals. (F) Current spikes (top) and conductivity changes (bottom) of PFM in phosphate-buffered saline (pH 7.4) with (blue) and without (red) 1 mM ATP under a 10-pulse train ($V = +0.5$ V, $\Delta t = t_p = 10$ ms). (G) Plots of current changes ($\Delta I/I_0 - I_t$) under a 10-pulse train ($V = +0.5$ V, $t_p = 10$ ms) with pulse intervals. (Inset) Values of retention time with (blue) and without (red) 1 mM ATP in solution. Error bars in (D), (E), and (G) present standard deviation of three measurements with the same device.

the chemical regulation of STP by different anions ($V = \pm 2$ V, $\Delta t = t_p = 10$ ms). Compared with that in NaCl aqueous solution (Fig. 3, B and C, red), the PFM in NaBF₄ solution exhibits stronger PPF and slightly attenuated PPD (Fig. 3, B and C, blue). Both effects were attenuated in NaClO₄ solution (Fig. 3, B and C, yellow). Moreover, t_r is related to the chemical environment, as revealed by the biexponential dynamic curve with different anion species (Fig. 3D and fig. S7A). The value of t_r decreases in the order of $t_{r,\text{ClO}_4^-} < t_{r,\text{BF}_4^-} < t_{r,\text{Cl}^-}$ both for positive and negative voltage pulse stimulation (table S1). In addition, the STP performance of the PFM could be regulated by the ionic strength. High-concentration electrolyte accelerates the disappearance of STP (the lower t_r) under either positive or negative voltage pulse stimulation (Fig. 3E, fig. S7B, and table S1).

To provide in-depth insights into the mechanism of this dependence between ion species or concentration and STP performance of the PFM, we used the Dukhin number at the pipette tip (D_u_0) to evaluate the surface conductivity changes in the system. Larger D_u_0 indicates that there are more anions partici-

pating in the ion redistribution to intensify memristive effect, and vice versa. The influence of Pim-anion interactions on D_u_0 at steady state without bias voltages is described by the following equation

$$D_u_0 = KC_A^{-1} \left(1 + \frac{k_2}{k_1} C_A \right)^{-1} \quad (2)$$

where, K is a structural constant of the PFM, C_A is the anion concentration of electrolyte, and k_1 and k_2 are the dissociation and association kinetic constants, respectively (see supplementary text). Here, the value of k_2/k_1 is closely related to the hydration energy of anions (25). For anions with a larger hydration energy, the value of k_2/k_1 would be lower, yielding a larger value of D_u_0 . The Cl⁻ bears the highest hydration energy ($\Delta H_{\text{Hyd},\text{ClO}_4^-}^0 < \Delta H_{\text{Hyd},\text{BF}_4^-}^0 < \Delta H_{\text{Hyd},\text{Cl}^-}^0$) and thus the largest value of D_u_0 . That is, more free Cl⁻ counterions in the PimB layer participate in the redistribution process (Fig. 3D, inset, top), resulting in longer retention time ($t_{r,\text{ClO}_4^-} < t_{r,\text{BF}_4^-} < t_{r,\text{Cl}^-}$). For ions with lower hydration energy, such as BF₄⁻ and ClO₄⁻, the increased k_2/k_1 value results in a smaller D_u_0 . This means that more

BF₄⁻ and ClO₄⁻ counterions in the PimB layer exist in the form of imidazolium-anion (PimA) pairs than do Cl⁻ counterions, resulting in a decrease of mobile anions participating in the ion redistribution in the PFM (Fig. 3D, inset, bottom, and supplementary text), and consequently the shorter retention time. Increasing the ion concentration also leads to the D_u_0 decrease according to Eq. 2, explaining the change of retention time with ion strength. These chemical-regulated STP changes hold promise for the possibility of realizing neuromorphic functions with the synergism of multiple ion species, which is almost impossible for solid-state systems.

We further exploited bioactive molecules to modulate STP patterns in a complex environment stimulated by mild voltage pulses. In a physiological electrolyte (i.e., phosphate-buffered saline solution, pH 7.4), the PFM maintains its STP characteristic under the stimulation of 10 voltage pulses ($V = +0.5$ V, $\Delta t = t_p = 10$ ms) (Fig. 3F, red), validating the PFM in biological environment. More importantly, when 1 mM adenosine triphosphate (ATP) was added into the solution, reduced conductivity changes were observed (Fig. 3F),

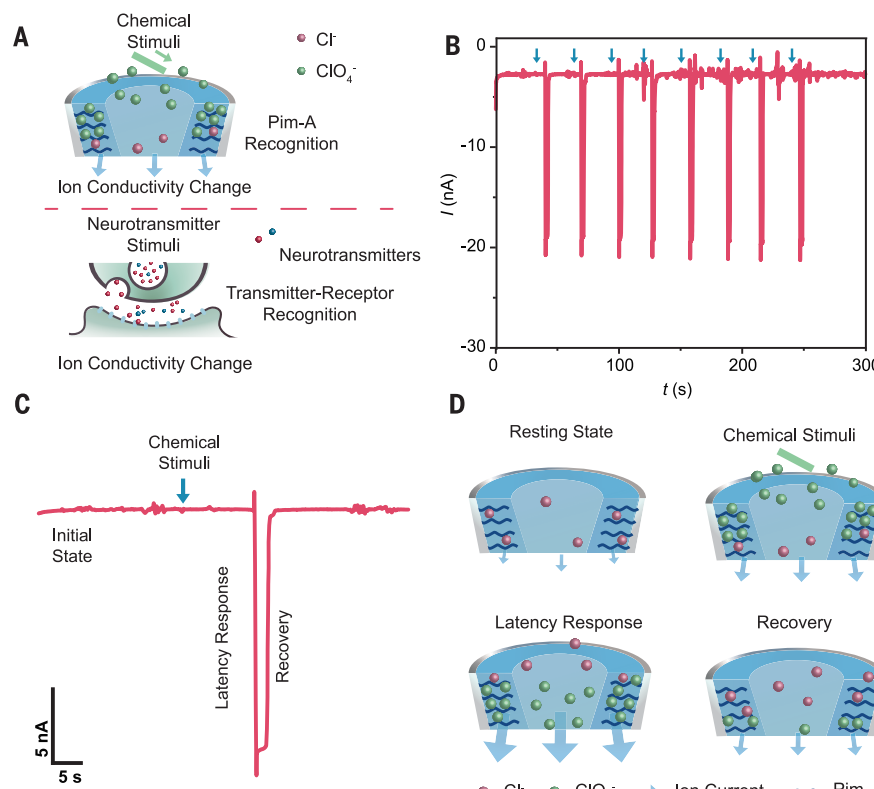


Fig. 4. Chemical-electric signal transduction of PFM. (A) Schematic illustration of the chemical-electric transduction of PFM (top) and biological synapses (bottom). (B) Electric pulse response of PFM under the stimulation of ClO₄⁻. The blue arrows indicate the delivery of ClO₄⁻. (C) Zoom-in of a single electric pulse. (D) Schematic illustration of the ion distribution changes in the PFM when chemical stimuli were delivered into the system.

along with a change in retention time from 156 ms to 138 ms (Fig. 3G). This phenomenon can also be well understood by Eq. 2 owing to the strong interaction of ATP with Pim (34). As indicated, the PFM may allow direct interfacing and communicating with biological systems, given that its neuroplastic behaviors are controllable by bioactive molecules.

Chemical-electric signal transduction with PFM

For biological systems, signal transduction at chemical synapses is mediated by the release and recognition of neurotransmitters (35) (Fig. 4A). Such a process is almost impossible to emulate with solid-state memristors, which hardly respond to external chemical stimulations. For fluidic-based devices with easily adaptable configurations, however, this chemical-electric signal transduction may be realized by tuning the behaviors of multiple ion species in the PimB-confined channel.

To achieve this target, a capillary controlled by a microinjector pump was inserted into the inner solution of the PFM, serving as the pre-synaptic neuron for the delivery of chemical stimuli. Herein, ClO₄⁻ was chosen as an “arti-

ficial neurotransmitter” for demonstration (Fig. 4A, top). When the chemical stimulus (ClO₄⁻) was back-injected into the micropipette, a responsive electric pulse was observed (Fig. 4B), analogous to neural spikes induced by a neurotransmitter. Under a negative bias voltage (-1 V), the PFM holds at a low conductive state owing to the low anion concentration in the PimB layer, emulating the resting state of neurons. When the ClO₄⁻ anions were released from the capillary and transported to the sensitive tip region driven by electrophoresis and convective flow, formation of Pim-ClO₄⁻ pairs due to the stronger interaction between Pim and ClO₄⁻ would decrease the effective surface charge density, further hindering the depletion of anions in PimB layers, resulting in the increase of ion current under negative voltage (25, 26). This phenomenon is similar to the opening of postsynaptic ion channels activated by neurotransmitters. Then, electrophoresis and electroosmotic flow drive Cl⁻ ions moving toward the tip, and the subsequent dissociation of Pim-ClO₄⁻ pairs brings the current back to the initial state, emulating the clearance of transmitters (Fig. 4, C and D). In comparison,

no current spike occurs after injection of pure NaCl solution with the same stimulation time (fig. S8A). The PFM shows the capability of individually accomplishing transduction from chemical stimuli of certain species to electric pulse signals.

Moreover, the ion current pulses induced by chemical stimulation show typical spiking latency behavior. A time lapse was observed between the stimulation and the occurrence of neuromorphic spikes (Fig. 4, B and C). When stimulation intensity increases, the time lapse decreases accordingly (fig. S8, B and C). The spiking latency behavior in real neurons plays a key role in encoding input strength with spike timing (36), this result thus provides the possibility for encoding chemical stimulations based on PFM.

Discussion

In this work, we have experimentally demonstrated a fluidic memristor with neuromorphic functions by using polyelectrolyte-confined fluidic structure, which features the typical fingerprints of a memristor. The time-dependent ion redistribution controlled by Pim-anion interactions under spatial confinement contributes to the ion memory. The as-fabricated PFM features the powerful ability to mimic STP electric pulse patterns with retention time and energy consumption comparable to those of the ion channels in biological systems. More importantly, the fluidic-based ion redistribution dynamics can endow the PFMs with neuromorphic function versatility that is hardly achievable with solid-state devices, offering the opportunity to introduce specific chemical regulation pathways to neuromorphic functions. Even more impressively, the emulation of chemical-electric signal transduction can be accomplished with this device. Compared with neuromorphic devices based on other mechanisms, our fluidic-based device offers not only performances comparable to biological systems but also more advanced neuromorphic functionalities, especially chemical-related functions (table S2).

Although the as-presented PFM features a series of advantages—diversity in neuromorphic functions, the possibility of regulation and coexistence of multiple ion carriers, and convenient interfacing with biological systems—big challenges remain on the way toward realizing broader applications for PFMs. For example, realizing long-term plasticity functions is a key goal for fluidic-based systems, where the introduction of much stronger (even irreversible) interfacial recognition interactions (e.g., aptamers toward substrates) would be potentially helpful for prolonging ion memory. The scale-up of fluidic memristors for in-memory computing is another challenge, for which porous micro- or nanofluidic arrays might offer a solution.

REFERENCES AND NOTES

1. Z. Wang *et al.*, *Nat. Rev. Mater.* **5**, 173–195 (2020).
2. M. A. Zidan, J. P. Strachan, W. D. Lu, *Nat. Electron.* **1**, 22–29 (2018).
3. Y. Lee *et al.*, *Sci. Adv.* **4**, eaat7387 (2018).
4. X. Zhang *et al.*, *Nat. Commun.* **11**, 51 (2020).
5. S. T. Keene *et al.*, *Nat. Mater.* **19**, 969–973 (2020).
6. T. Wang *et al.*, *Nat. Electron.* **5**, 586–595 (2022).
7. Y. Kim *et al.*, *Science* **360**, 998–1003 (2018).
8. S. Kim *et al.*, *Sci. Adv.* **7**, eabe3996 (2021).
9. D. B. Strukov, G. S. Snider, D. R. Stewart, R. S. Williams, *Nature* **453**, 80–83 (2008).
10. Z. Wang *et al.*, *Nat. Mater.* **16**, 101–108 (2017).
11. Q. Xia, J. J. Yang, *Nat. Mater.* **18**, 309–323 (2019).
12. Y. van de Burgt *et al.*, *Nat. Mater.* **16**, 414–418 (2017).
13. E. J. Fuller *et al.*, *Science* **364**, 570–574 (2019).
14. C. E. G. Hoskin, V. R. Schild, J. Vinals, H. Bayley, *Nat. Chem.* **14**, 650–657 (2022).
15. C. Wei, A. J. Bard, S. W. Feldberg, *Anal. Chem.* **69**, 4627–4633 (1997).
16. R. A. Lucas, C.-Y. Lin, L. A. Baker, Z. S. Siwy, *Nat. Commun.* **11**, 1568 (2020).
17. M. R. Powell, L. Cleary, M. Davenport, K. J. Shea, Z. S. Siwy, *Nat. Nanotechnol.* **6**, 798–802 (2011).
18. D. Wang *et al.*, *J. Am. Chem. Soc.* **134**, 3651–3654 (2012).
19. Q. Sheng, Y. Xie, J. Li, X. Wang, J. Xue, *Chem. Commun.* **53**, 6125–6127 (2017).
20. J. S. Najem *et al.*, *ACS Nano* **12**, 4702–4711 (2018).
21. P. Zhang *et al.*, *Nano Lett.* **19**, 4279–4286 (2019).
22. P. Robin, N. Kavokine, L. Bocquet, *Science* **373**, 687–691 (2021).
23. P. Robin *et al.*, arXiv:2205.07653 [cond-mat.soft] (2022).
24. V. M. Ho, J.-A. Lee, K. C. Martin, *Science* **334**, 623–628 (2011).
25. X. He *et al.*, *Angew. Chem. Int. Ed.* **57**, 4590–4593 (2018).
26. X. He *et al.*, *J. Am. Chem. Soc.* **139**, 1396–1399 (2017).
27. L. Chua, *IEEE Trans. Circuit Theory* **18**, 507–519 (1971).
28. D. Wang *et al.*, *ChemElectroChem* **5**, 3089–3095 (2018).
29. L. Chua, G. Ch. Sirakoulis, A. Adamatzky, Eds., *Handbook of Memristor Networks* (Springer, 2019).
30. R. S. Zucker, W. G. Regehr, *Annu. Rev. Physiol.* **64**, 355–405 (2002).
31. S. B. Laughlin, R. R. de Ruyter van Steveninck, J. C. Anderson, *Nat. Neurosci.* **1**, 36–41 (1998).
32. D. Stellwagen, R. C. Malenka, *Nature* **440**, 1054–1059 (2006).
33. H. Thoenen, *Science* **270**, 593–598 (1995).
34. K. Zhang *et al.*, *Sci. China Chem.* **63**, 1004–1011 (2020).
35. A. E. Pereda, *Nat. Rev. Neurosci.* **15**, 250–263 (2014).
36. E. M. Izhikevich, *IEEE Trans. Neural Netw.* **15**, 1063–1070 (2004).
37. T. Xiong *et al.*, Data for: Neuromorphic functions with a polyelectrolyte-confined fluidic memristor, Dryad (2022); <https://doi.org/10.5061/dryad.d2547d85r>.

ACKNOWLEDGMENTS

We are grateful to the anonymous reviewers for their thoughtful comments and advice on improving this manuscript. **Funding:** Funding was provided by National Natural Science Foundation of China grants 21790390, 21790391, and 22134002 (L.M.); 22125406, 21790053, and 22074149 (P.Y.); and 22222411 (F.W.). Funding was also provided by the Natural Science Foundation

of Beijing (JQ19009), the Strategic Priority Research Program of the Chinese Academy of Sciences (XDB30000000), and the CAS Project for Young Scientist in Basic Research (YSBR-050).

Author contributions: Conceptualization: P.Y. and L.M. Supervision: P.Y. and L.M. Funding acquisition: F.W., P.Y., and L.M. Methodology: T.X., F.W., W.M., Y.J., P.Y., and L.M. Investigation: T.X., C.L., X.H., B.X., and J.Z. Visualization: T.X., C.L., X.H., B.X., F.W., W.M., Y.J., and J.F. Writing – original draft: T.X. and P.Y. Writing – review: T.X., F.W., P.Y., and L.M.

Competing interests: The authors declare no competing interests.

Data and materials availability: All data needed to evaluate the conclusions in the paper are present in the main text or the supplementary materials. The tabulated numerical data underlying the figures and the model for FEM simulation are deposited in Dryad (37). **License information:** Copyright © 2023 the authors, some rights reserved; exclusive licensee American Association for the Advancement of Science. No claim to original US government works. <https://www.science.org/about/science-licenses-journal-article-reuse>

SUPPLEMENTARY MATERIALS

science.org/doi/10.1126/science.adc9150
Materials and Methods
Supplementary Text
Figs. S1 to S8
Tables S1 and S2
References (38–47)

Submitted 9 May 2022; accepted 10 November 2022
[10.1126/science.adc9150](https://doi.org/10.1126/science.adc9150)